

Corrosion properties of plasma electrolytic oxidation coatings on an aluminium alloy – The effect of the PEO process stage



Vahid Dehnavi ^{a,*}, David W. Shoesmith ^b, Ben Li Luan ^{c,d}, Mehdi Yari ^d, Xing Yang Liu ^c, Sohrab Rohani ^a

^a Department of Chemical and Biochemical Engineering, University of Western Ontario, London, N6A 5B9 ON, Canada

^b Surface Science Western, Department of Chemistry, University of Western Ontario, London, N6A 5B7 ON, Canada

^c National Research Council Canada, 800 Collip Circle, London, N6G 4X8 ON, Canada

^d Department of Chemistry, University of Western Ontario, London, N6A 5B7 ON, Canada

HIGHLIGHTS

- Corrosion performance of PEO coatings was found to be dependent on coating stage.
- The PEO stage determined by the process parameters controlled coatings morphology.
- Samples coated at the end of stage 3 demonstrated better corrosion properties.
- Coating thickness and phase composition showed no influence on corrosion resistance.

ARTICLE INFO

Article history:

Received 24 November 2014

Received in revised form

7 April 2015

Accepted 30 April 2015

Available online 26 May 2015

Keywords:

Ceramics

Coatings

Plasma deposition

Electron microscopy

Corrosion

Microstructure

ABSTRACT

Plasma electrolytic oxidation (PEO) coatings were grown on an aluminium alloy substrate using different processing parameters which enabled samples to be coated to different stages of the PEO process. Electrochemical impedance spectroscopy (EIS) and linear polarization resistance (LPR) techniques were employed to investigate the impedance properties of the resulting oxide coatings which will determine the corrosion performance of the coated alloy. Scanning electron microscopy was used to relate the morphology of the coatings with their corrosion performance. A direct relationship was found between the stage of the PEO process, which affects the microstructure of the coatings, and the corrosion performance. Coating thickness and phase composition did not have any measurable influence on coating corrosion performance. To some degree corrosion performance could be tailored by the processing parameters.

Crown Copyright © 2015 Published by Elsevier B.V. All rights reserved.

1. Introduction

Plasma electrolytic oxidation (PEO) has attracted a lot of interest as a relatively novel surface engineering technology with great potential in different industrial applications. PEO is considered an environmentally friendly coating process mainly focused on the improvement of the wear and corrosion resistance of valve metals

including aluminium, magnesium, titanium, zirconium and their alloys [1–5].

The configuration used in the PEO process is similar to conventional anodizing. The sample is immersed in an aqueous electrolyte but compared to anodizing, a much higher potential (~400–700 V) is applied during PEO resulting in the formation of many electrical micro-discharges (plasma plume) caused by the localized dielectric breakdown of the growing oxide coating [6,7]. These micro-discharges are discrete and short-lived and play an important role in the formation of the coating phase composition, structure and morphology [8].

The characteristics of PEO coatings could be influenced by applying different processing parameters including the applied

* Corresponding author.

E-mail addresses: vdehnavi@uwo.ca, vdehnavi@gmail.com (V. Dehnavi), dwshoesm@uwo.ca (D.W. Shoesmith), Ben.Luan@nrc-cnrc.gc.ca (B.L. Luan), myari@uwo.ca (M. Yari), XingYang.Liu@nrc-cnrc.gc.ca (X.Y. Liu), srohani@uwo.ca (S. Rohani).

power mode, electrolyte composition, deposition time, and substrate chemical composition [9,10]. Prior studies have extensively investigated the effects of processing parameters on the properties of PEO coatings on aluminium alloy substrates. Current operating modes were found to significantly affect the aluminium oxide coating morphology and microstructure. A bipolar pulsed DC mode, as opposed to a unipolar current mode, was found to improve the coating quality and produce denser coatings with enhanced morphology and cross-sectional microstructure [11]. Changing the current mode from unipolar to bipolar was reported to improve the corrosion resistance of a magnesium alloy [12]. The enhanced properties of coatings prepared using the pulsed bipolar current mode were ascribed to the reduced number of strong plasma discharges during the PEO process.

The micro-discharge behaviour and coating growth process are also thought to be changed by the applied duty cycle, frequency and current density, which in turn would determine the composition, microstructure and morphology, as well as mechanical and tribological properties of the PEO coatings [6,8,10,13,14]. Lower duty cycles and higher frequencies were reported to produce micro-discharges with higher spatial density and lower intensity resulting in a lower concentration of Si on the surface of the coatings, which were composed of mainly γ -Al₂O₃ on aluminium alloy substrates [6]. Application of higher current density and duty cycle generally increase the coating thickness and enhance the $\gamma \rightarrow \alpha$ -Al₂O₃ phase transformation [8,10].

The electrolyte used in PEO is typically a low concentration alkaline solution free of heavy metals (Cr, Ni, V, etc.) and compared to hard anodizing, where strong acids are employed, is much more environmentally friendly [15]. The wastewater from PEO treatment can also be used to produce value added products, such as zeolite [16]. An extremely wide range of electrolyte compositions has been used for PEO coatings. Electrolytes used in the PEO of Al alloys are typically silicate and phosphate based aqueous solutions with organic and inorganic additives to further improve the properties of the coatings [17,18]. Increasing the sodium silicate content of the electrolyte enhances the growth rate, which may be attributed to the incorporation of more silicate into the coating structure, and promotes the formation of Si-rich species on the coating surface [19]. Increasing the alkali concentration is believed to lead to local dissolution of oxides thus decreasing the coating growth rate [20].

In recent years the effect of different processing parameters on the corrosion behaviour of PEO coatings has been investigated. Bajat et al. [21] studied the influence of PEO treatment time on the corrosion stability of oxide coatings on aluminium in sodium tungstate and observed that neither the concentration of tungsten in the coating, nor the coating thickness were the governing factors in the corrosion stability of the coatings. Hussein et al. [1] investigated the effect of PEO deposition time and substrate composition on the corrosion resistance of Mg alloys and concluded that surface morphologies, coating thickness and porosity level varied with both treatment time and substrate composition and influenced the corrosion behaviour.

Given the multiple processing parameters that affect PEO and the wide range within which they can be varied, it is extremely difficult to find the optimum combination of parameters to achieve the best corrosion resistance. A more systematic approach is required to determine the role of processing parameters on corrosion if these coatings are to be industrially applied.

The surface morphology and coating microstructure have been found to play a significant role in determining corrosion by influencing the amount and size of defects such as porosity and microcracks in the coatings [1]. A recent study [22] suggested that applying different electrical parameters including frequency, duty cycle and current density affected the voltage-time behaviour, and

changed the duration and ratio of PEO treatment stages. A correlation was established between surface morphology, microstructure, and the stages within the voltage-time curve. This study presents an investigation of the corrosion behaviour of an Al alloy coated in different PEO treatment stages and investigates the influence of different processing parameters including frequency, duty cycle, current density and time.

2. Materials and methods

2.1. Materials

The substrate material used in the present investigation was the 6061-T651 aluminium alloy with a nominal chemical composition of (wt%): 0.40–0.80% Si, 0.70% Fe, 0.15–0.40% Cu, 0.15% Mn, 0.80–1.20% Mg, 0.04–0.35% Cr, 0.25% Zn, 0.15% Ti, and balance Al. Specimens in the shape of coupons with a thickness of 6–8 mm and a diameter of ~30 mm were ground with abrasive papers up to 600 grit, washed in propanol, rinsed with distilled water, and dried.

2.2. PEO coating process

An alkaline silicate solution (2 g/l KOH, 2 g/l Na₂SiO₃ in distilled water) held in a stainless steel container was used as the electrolyte. Aluminium coupons, connected to the positive output of the power supply, served as the working electrode (anode) and the stainless steel container as the counter electrode (cathode). The coating process was carried out at constant current densities (J) of 10, 15, and 20 A/dm² using a unipolar pulsed DC mode with a square waveform applied at different frequencies of 50 and 1000 Hz. Two duty cycles (D_t) of 20% and 80% were used. The temperature of the electrolyte was maintained between 20 and 30 °C throughout the coating process using a heat exchanger. Samples were coated for 30 min. The PEO process parameters and sample codes used in this study are listed in Table 1.

2.3. Coating characterization

Coating thickness was evaluated using an Eddy current gauge. Twenty measurements were taken on each coated sample and the average coating thickness and the statistical error calculated. Surface morphologies and cross-sections of the coatings were examined using a Hitachi S-3500N and a LEO 440 scanning electron microscope (SEM) equipped with a Quartz EDX system.

2.4. Electrochemical experiments

Linear polarization resistance (LPR) and electrochemical impedance spectroscopy (EIS) measurements were carried out at room temperature in a 3.5 wt.% NaCl solution. Measurements were made after allowing the sample to stabilize at the corrosion potential (E_{corr}) for 2 h. A standard three-electrode cell arrangement was used with the coated samples serving as the working electrode, with a platinum plate as the counter electrode, and a saturated calomel reference electrode (SCE). The cell was housed inside a

Table 1
PEO process parameters and sample codes for coatings deposited on 6061 aluminium alloy substrates.

Sample code	Frequency (Hz)	D_t (%)	*: J (A/dm ²)
S12-*	1000	20	10, 15, 20
S18-*	1000	80	
S52-*	50	20	
S58-*	50	80	

Faraday cage to reduce electrical noise from external sources. Electrochemical measurements were made using a 1287 Solartron potentiostat and a Solartron 1255B frequency response analyzer connected to a computer equipped with Corrware software.

Polarization resistance (R_p) values were determined by scanning the potential over a range of ± 0.02 V with respect to E_{corr} at a sweep rate of 1.0 mV/s. EIS data were obtained at E_{corr} using a sinusoidal input potential with an amplitude of ± 10 mV over the frequency range of 10^{-1} – 10^3 Hz. EIS data were analyzed by fitting to an appropriate electrical equivalent circuit using ZView electrochemical analysis software. All electrochemical experiments were repeated three times to verify their reproducibility.

3. Results and discussion

3.1. Voltage-time response and corrosion properties

The impedance properties of PEO coatings prepared using different electrical parameters were investigated by EIS and LPR. EIS can provide useful information on the corrosion performance of the PEO coatings and on the resistance of the aluminium oxide coating to water and ionic transport [23].

PEO coatings may be comprised of up to three layers, depending on the processing conditions employed; a thin barrier layer close to the substrate, an intermediate or functional layer with relatively low porosity, and a porous, loose outer layer [17,24]. The barrier layer is thought to be the major contributor to corrosion protection while the functional layer has high hardness, depending on the processing conditions and the substrate used, and can provide protection against wear [25]. PEO coatings produced under the conditions used in this study were previously verified to consist of two layers, the barrier and the functional layers with a patchy third outer loose layer on some samples coated at higher current densities. Pores, which were connected in some areas and possibly enlarged during sample preparation and polishing, were observed between the functional and inner layer of the coatings [22].

Nyquist plots recorded on Al alloy substrates coated at 1000 Hz and 50 Hz are presented in Fig. 1 and Fig. 2, respectively. As commonly observed [21,26–28], the spectra exhibit two time constants, representative of the dual layer coatings [29]. The high frequency time constant (CPE1-R1) is attributed to the functional layer, and the second lower frequency time constant (CPE2-R2) to the inner barrier layer, Figs. 1 and 2.

EIS data is commonly analyzed by fitting it to an equivalent electrical circuit model consisting of different common electrical elements. The impedance data in this study can be interpreted in terms of the demonstrated structure of PEO coatings on the 6061 Al alloy [6,22] and on previous studies on the corrosion resistance of PEO coatings using the equivalent circuit presented in Fig. 3 [30–34].

The spectra were fitted to this circuit using non-linear least squares analysis software. In this circuit, R_s represents the solution resistance between the PEO-coated sample (working electrode) and the reference electrode. The value of R_s depends primarily on the geometry of the electrochemical cell and the conductivity of the test solution and the values obtained from the fitted spectra were consistently small ($<100 \Omega \text{ cm}^2$).

In the equivalent circuit in Fig. 3, R_1 represents the resistance of the pores and defects, such as the discharge channels in the outer functional layer of the PEO coating and is in parallel with a constant phase element, CPE1. The use of the more general constant phase element (CPE) to represent the capacitance of this functional layer yields a better fit of the experimental data [28,34].

The impedance of a CPE can be expressed by the following equation:

$$Z_{\text{CPE}} = 1/[Q(j\omega)^n] \quad (1)$$

in which Q is the CPE constant, j is the imaginary unit ($\sqrt{-1}$), ω is the angular frequency (rad/s) of the sine wave defined as $\omega=2\pi f$, f is the frequency in Hz, and n is an exponent representing the physical meaning of the CPE and ranges between 0 and 1. A value of zero for n implies pure resistance and a value of 1 ($n=1$) pure capacitance. Values of n in the range $0.25 < n < 0.5$ may indicate an impedance associated with mass transport, i.e., a Warburg impedance. Deviations of n from these values indicates the non-ideality of the system [1,34]. R_2 and CPE2 represent the resistance and constant phase element for the barrier layer, respectively. Given the patchy loose nature of the porous outer layer, it is unlikely to influence the impedance of the coating and is not represented by elements in the electrical equivalent circuit. It was previously shown that this layer was composed of widely dispersed clusters of particles which do not block a significant number of pores in the functional layer [22].

The values of the circuit elements obtained from fits to the spectra are summarized in Table 2. The quality of the fittings was evaluated based on the chi-squared (χ^2) values. Chi-squared is the

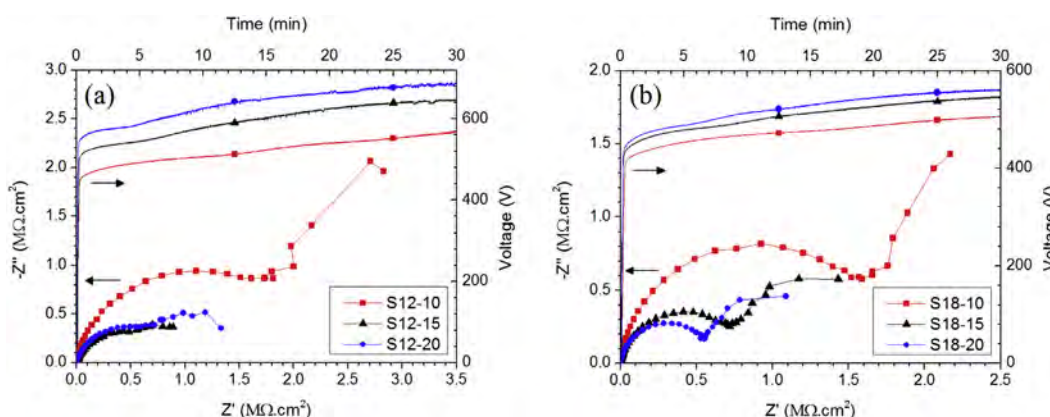


Fig. 1. Voltage-time curves and Nyquist plots for PEO coatings on 6061 Al alloy substrates prepared using different electrical parameters; (a) S12-* samples, (b) S18-* samples (Table 1). The frequencies at which the last point of the first arc was recorded for S12-10, S12-15, and S12-20 samples are 1.23, 0.43, and 0.81 Hz, respectively and for S18-10, S18-15, and S18-20 are 0.53, 1, and 1 Hz, respectively.

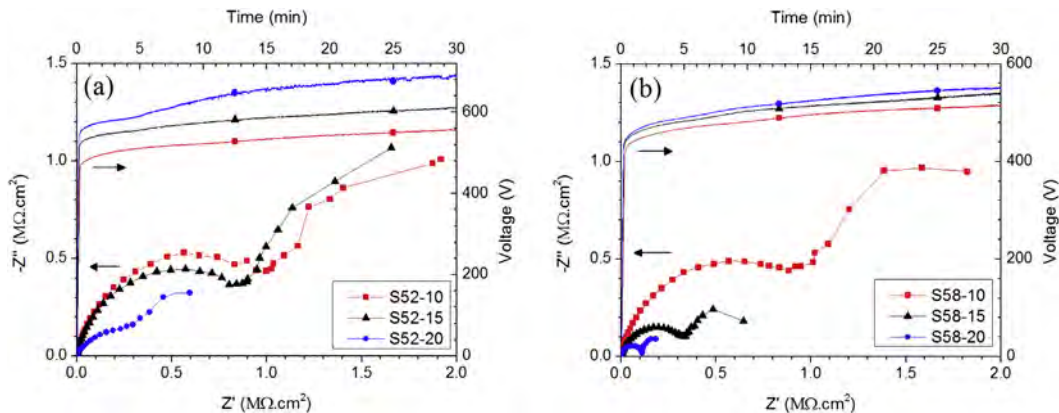


Fig. 2. Voltage-time curves and Nyquist plots for PEO coatings on 6061 Al alloy substrates prepared using different electrical parameters; (a) S52-* samples, (b) S58-* samples (Table 1). The frequencies at which the last point of the first arc was recorded for S52-10, S52-15, and S52-20 samples are 0.81, 0.43, and 1.23 Hz, respectively, and for S58-10, S58-15, and S58-20 are 0.81, 1, and 1.23 Hz, respectively.

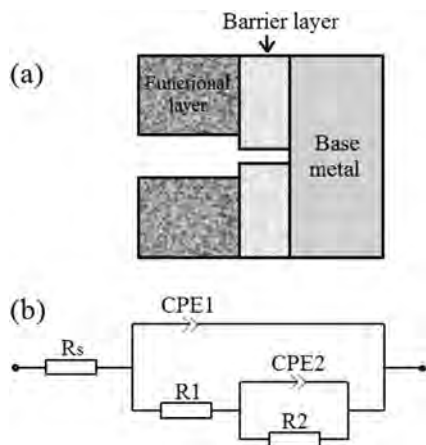


Fig. 3. Schematic representation of PEO-coated 6061 Al alloy (a); and the equivalent circuit (b) used to model the EIS data recorded in 3.5 wt% NaCl solution.

square of the standard deviation between the original data and the calculated spectrum and the lower the values, the better the fitting. The chi-squared values were in the range 3×10^{-4} – 1×10^{-3} indicating good agreement between the experimental data and equivalent circuit fits. The exponent n for the two CPEs was generally >0.85 for CPE1 and commonly close to 1 for CPE2 confirming the generally capacitative behaviour of the two layers.

The E_{corr} values obtained on the coated samples, measured prior to LPR (R_p) measurements, were in the range –773––732 mV compared to a value of –745 mV on an uncoated sample. The R_p values from the LPR measurements are in generally good agreement with R_p values obtained from EIS measurements ($R_1 + R_2$) confirming the validity of the latter values despite the limited amount of low frequency data.

The R_p values are plotted in Fig. 4 for the various conditions used in producing the coatings. The average R_p value for the untreated alloy was $0.021 \text{ M}\omega\text{.cm}^2$, while for the S18-10 sample the maximum average R_p value was $4.28 \text{ M}\omega\text{.cm}^2$ indicating a nearly 200-fold improvement in corrosion resistance. The parameter values obtained by fitting the EIS spectra show the resistance of the inner barrier layer, R_2 , is generally higher than that of the outer functional layer, R_1 , indicating that it contributes most to the overall coating corrosion resistance. The higher corrosion resistance properties of the barrier layer compared to the outer functional layer have been previously reported [21,30,35].

The voltage-time response curves and Nyquist plots for different groups of samples coated using different electrical parameters are presented together in Figs. 1 and 2. During the PEO process, up to four stages can be observed in the voltage-time curves. A schematic PEO voltage-time response curve is presented in Fig. 5. During stage 1 which is similar to conventional anodic oxidation, the voltage increases rapidly within a short time as the result of electrochemical formation of aluminium oxide on the substrate. At the beginning of stage 2, the breakdown voltage is reached and white

Table 2
Linear polarization resistance (R_p) values and the values of parameters obtained from fitted EIS plots for PEO coatings on the 6061 Al alloy treated for 30 min under different electrical conditions (Table 1).

Sample	CPE1-Q ($\mu\text{F}/\text{cm}^2 \text{ s}^{n-1}$)	CPE1-n	$R_1 (\text{M}\Omega \text{ cm}^2)$	CPE2-Q ($\mu\text{F}/\text{cm}^2 \text{ s}^{n-1}$)	CPE2-n	$R_2 (\text{M}\Omega \text{ cm}^2)$	$R_p (\text{M}\Omega \text{ cm}^2)$ ^a
Bare Al	—	—	—	—	—	—	0.021
S12-10	0.046	0.90	2.181	0.622	~1	3.713	3.114
S12-15	0.347	0.79	0.882	3.241	~1	0.374	1.058
S12-20	0.174	0.83	0.989	1.729	~1	1.004	1.305
S18-10	0.036	0.93	1.788	0.953	0.99	3.836	4.281
S18-15	0.063	0.88	0.837	1.341	~1	0.885	1.288
S18-20	0.071	0.92	0.628	2.063	~1	0.631	0.841
S52-10	0.742	0.89	1.253	1.009	~1	1.374	1.536
S52-15	0.076	0.86	1.881	0.510	0.99	2.817	2.678
S52-20	0.374	0.72	0.360	2.330	0.84	0.774	0.615
S58-10	0.078	0.88	1.165	1.037	~1	1.545	1.615
S58-15	0.118	0.86	0.375	0.329	~1	0.348	0.791
S58-20	0.169	0.93	0.123	12.887	~1	0.132	0.354

^a Extracted from linear polarization test results.

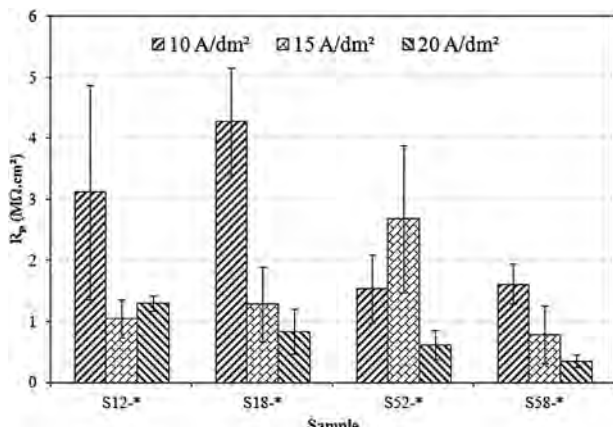


Fig. 4. Polarization resistance (R_p) values calculated from LPR experiments on PEO coatings grown using different electrical parameters.

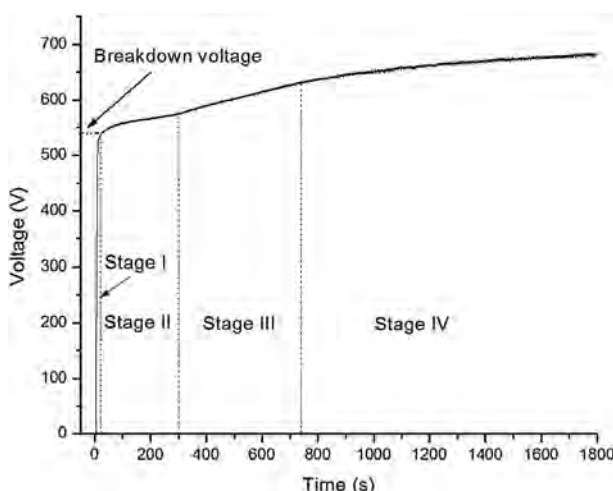


Fig. 5. Schematic of a voltage-time response curve containing the four stages observed during the PEO process.

sparks, distributed uniformly on the metal surface, appear. The slope of the voltage–time curve decreases substantially and intensive gas liberation is observed on the surface of the sample. In stage 3, the rate of voltage change increases slightly compared to stage 2, and the micro-discharges become more intense. In the final stage (4), the voltage increases more slowly with time and the sparks become even stronger and slower moving compared to stage 3 but their population decreases and they become more widely spaced [36–39]. It should be noted that while the transition from stage 1–2 is clear, the boundary between the two regions being sharp, the transitions from one stage to another is usually gradual and not necessarily as distinct as in the case presented in Fig. 5.

The characteristics of the electrical micro-discharges such as their population, size and colour as well as the coating surface morphology, microstructure, density and phase content are all affected by the stage of the PEO process [6,10,40]. The results of a recent study on PEO coatings on the 6061 Al alloy, prepared under similar conditions to those employed here [22], suggested a correlation existed between the stage of the PEO process and the microstructure and morphology of the coating. Applying different electrical parameters changed the duration of the PEO stages in the voltage–time response curve, and affected the coating growth rate,

surface morphology, microstructure and microhardness of the coatings. Applying higher current densities and lower duty cycles were found to decrease the length of stage 2 and increase the duration of the last two stages, while frequency did not significantly affect the duration of the stages.

From Table 2 it can be appreciated that for the S12 series the coating formed at the lowest current density (10 A/dm^2) has the highest overall polarization resistance (R_p) comprised of high barrier (R_1) and functional (R_2) layer resistances. Increasing the current density (S12-15 and S12-20) decreased the resistances by approximately similar values (Table 2, Fig. 4). Inspection of the voltage–time curves in Fig. 1-a shows that, after the 30 min coating period, S12-10 was at the beginning of stage 4 while S12-15 and S12-20 were both in stage 4. A similar trend with current density is observed for the S18 series, Table 2 and Fig. 1-b, the layer resistances, R_1 and R_2 , both being largest for the coating formed at the lowest current density.

Consistent with the S12 series, the voltage–time response, Fig. 1-b, shows the high resistance S18-10 coating was in stage 3, while the lower resistance coatings, S18-15 and S18-20, were in stage 4. It is also worth noting that the S18-20 coating with the lowest resistances spent more time in stage 4 than the S18-15 with a slightly higher coating resistance. Again similar trends are observed for the S52-* and S58-* series. The influence of the time spent in stage 4 is apparent, as illustrated by a comparison of S58-15 and S58-20, the latter exhibiting a less resistive coating having spent a longer period of time in stage 4.

3.2. Microstructure and thickness of coatings

The SEM micrographs of the free surfaces of the S12-* and S18-* samples, produced under different electrical conditions are presented in Fig. 6. The coating surfaces generally exhibit two types of morphology: (i) a significant portion of the surface is occupied by craters; volcano-like microstructures formed by individual micro-discharge events, (ii) and a nodular structure consisting of hollow particles. The cratered areas are mainly composed of oxidized aluminium and contain discharge channels in the form of central holes through which the molten material flowed out of the channel to rapidly solidify and create distinctive boundaries of solidified pools [6,41,42]. The results of a previous study [42] showed that the average size of the discharge channels, as well as the diameters of the craters, increased gradually as the treatment time was extended from 1 to 30 min.

The average thicknesses of the coatings produced using different electrical parameters are illustrated in Fig. 7. In each group of samples, increasing the current density at constant frequency and duty cycle resulted in a thicker coating. A detailed discussion on the effect of electrical parameters on the coating thickness and cross-sections has been published elsewhere [22].

The results indicate that increasing the thickness of the oxide coatings does not necessarily improve the corrosion performance of the samples. All samples coated at a current density of 20 A/dm^2 were thicker than samples coated at lower current densities (Fig. 7) although, as shown above, their corrosion performance was generally worse.

However, examination of the surface morphologies of the samples, Fig. 6, suggests a correlation between the microstructure of the coating and its corrosion performance. The coatings with the best corrosion resistance, S12-10 and S18-10, possess a large number of small craters, Fig. 6 (a and d), while increasing the current density throughout these two series, S12-* (Fig. 6, a and c) and S18-* (Fig. 6, d and f), resulted in a decreased number of craters but an increase in their size. The size of the craters reflects the strength of the micro-discharge, and the holes in the centre of these cratered

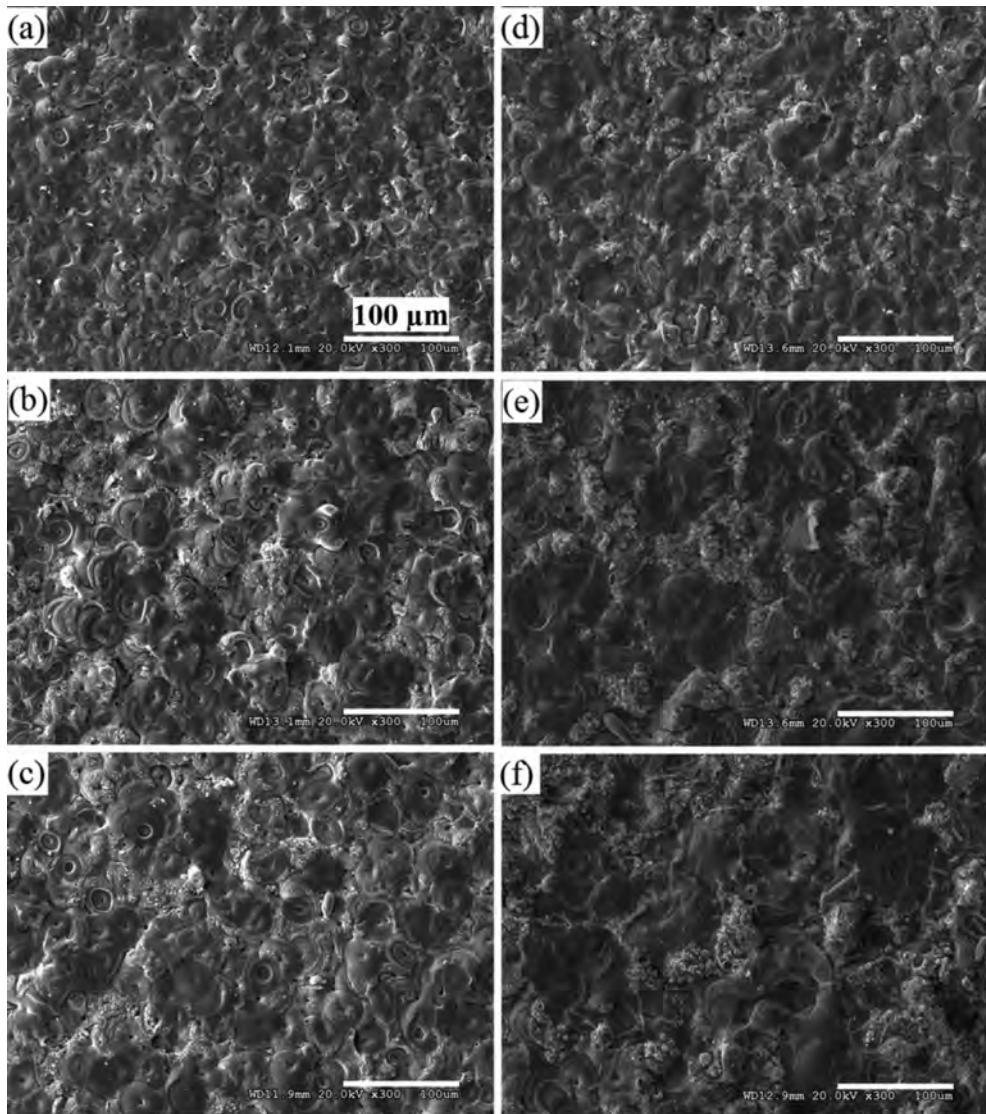


Fig. 6. SEM micrographs of the free surfaces of PEO coatings on 6061 Al alloys formed using different process parameters: (a) S12-10; (b) S12-15; (c) S12-20; (d) S18-10; (e) S18-15; and (f) S18-20 (Table 1).

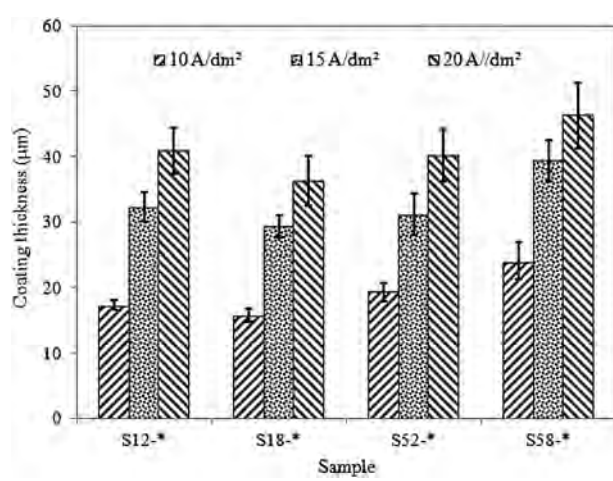


Fig. 7. Thickness of PEO coatings on 6061 Al alloy samples coated using different electrical parameters.

regions suggest they were formed as a result of these strong discharges. A possibility is that the holes penetrate deep in to the coating allowing access of the corrosive solution to the alloy surface [1].

Micro-discharges are generated by dielectric breakdown through weak sites in the PEO coating with the number of weak sites being reduced as the coating is thickened by growth at a higher current density and/or for longer deposition times. The increased size of the craters in thicker coatings, which is a reflection of stronger micro-discharges, could be ascribed to a reduced number of discharge sites through which current is able to pass. Under galvanostatic conditions this would lead to a higher current density at these locations. As the coating thickens, the diameter of the discharge channels increases because a higher energy is required for the current to pass through the thicker coating [43,44].

The characteristics of micro-discharges, which play a key role in the formation of the oxide coatings, vary during the different stages of the PEO process [22,45], and, as shown here, changes in electrical parameters can change the duration of the stages.

The coating corrosion resistance measurements showed that samples coated at the end of stage 3 and beginning of stage 4 generally demonstrated the highest corrosion resistance. This would be consistent with the surface morphology which consisted of small craters. Samples whose voltage-time curves had a longer stage 4 also had a lower corrosion resistance which can be related partly to the increased size of the discharge channels and access of the corrosive solution to deeper locations. However, the key role of the inner barrier layer should not be overlooked. The EIS results in

Table 2 show that, for almost all coatings, R_2 values, indicative of the corrosion resistance of the inner layer, are generally higher than R_1 values, the corrosion resistance of the outer layer, suggesting that the inner layer contributes most to the overall resistance of the coating. In addition, samples which spent more time in stage 4 generally show a lower value of R_2 .

Fig. 8 compares the SEM (back-scattered electron mode) and EDX elemental maps of the cross sections of S18–10 and S18–20 samples. S18–10, coated in stage 3, showed the highest overall

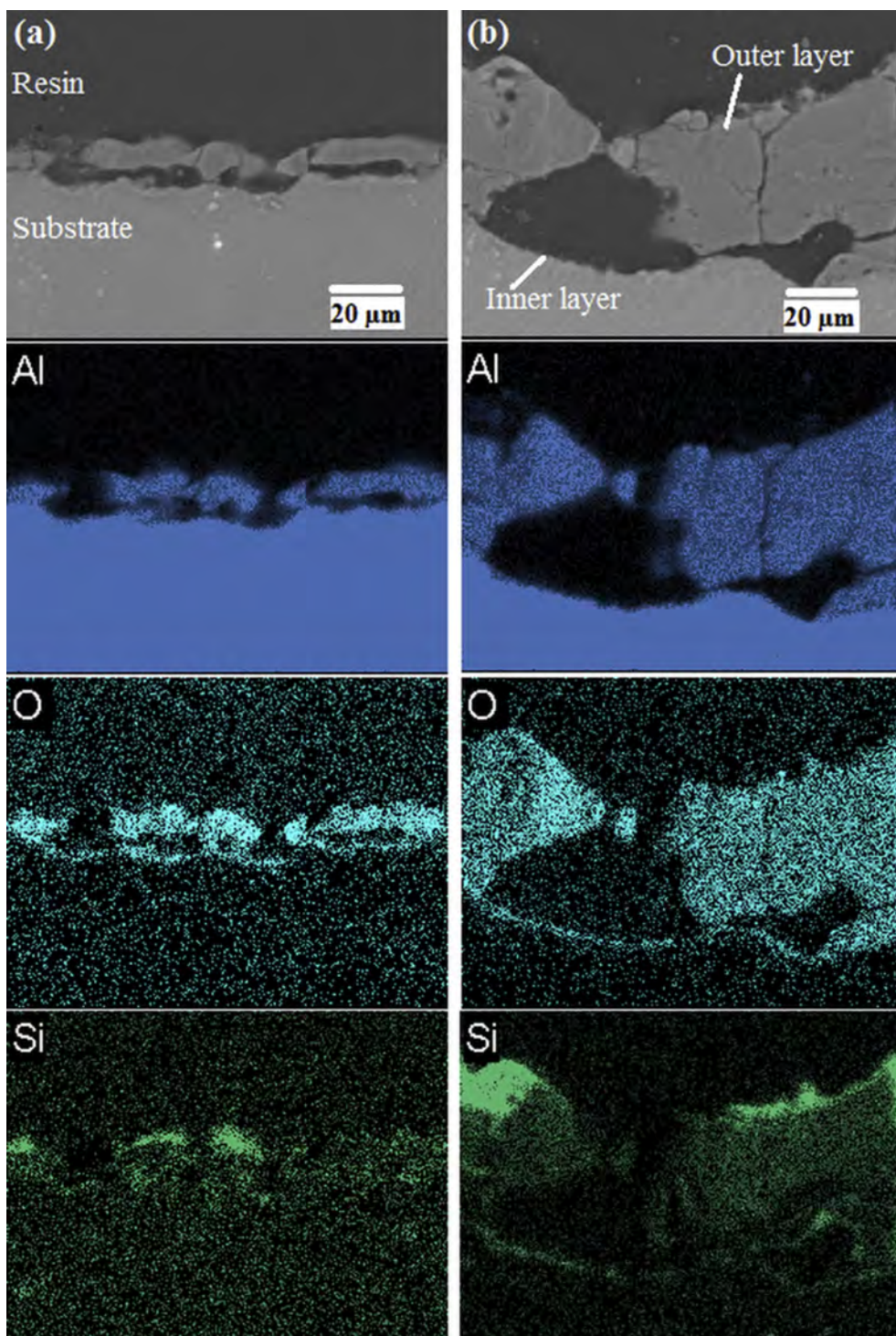


Fig. 8. SEM micrographs using back-scattered electron mode (BSE) and EDX elemental maps of polished cross sections of (a) S18–10 and (b) S18–20 samples.

corrosion resistance (Table 2) with R_p equal to $4.28 \text{ M}\Omega \text{ cm}^2$ and the maximum barrier layer resistance with R_2 equal $3.836 \text{ M}\Omega \text{ cm}^2$. For S18-20, coated in stage 4, the corresponding R_p and R_2 values were 0.841 and 0.631, respectively. The back-scattered SEM micrographs of S18-10 and S18-20, Fig. 8-a and Fig. 8-b, respectively, do not show the barrier layer very clearly, however, the EDX maps, mainly the ones for oxygen, clearly confirm the presence of an inner barrier layer for both coatings. Although the functional layer for S18-20, Fig. 8-b, is considerably thicker than that for S18-10, Fig. 8-a, the oxygen maps suggest the barrier layer of S18-20 is slightly thinner than S18-10. In addition, the EDX maps show there is a higher concentration of Si in the barrier layer in S18-20, suggesting once stage 4 is reached, silicate can degrade the properties of the barrier layer. These results suggest that the stage of the PEO process not only affects the coating surface morphology but the properties of the barrier layer too.

Re-examination of previous results on the influence of electrical growth parameters on the composition and transformation of phases within the coating [10] confirms that the phase composition does not play any significant role in coating corrosion performance. Despite the fact that the PEO coatings grown in this study contained different crystalline phases and had different thicknesses, coating microstructure and morphology seem to be the main factors in controlling the corrosion performance of the coatings.

3.3. Influence of PEO deposition time

To confirm the relationship between corrosion performance and the coating growth stage, a series of coatings were grown for different deposition times using the same electrical growth parameters. Based on the voltage-time response curve for the S12-15

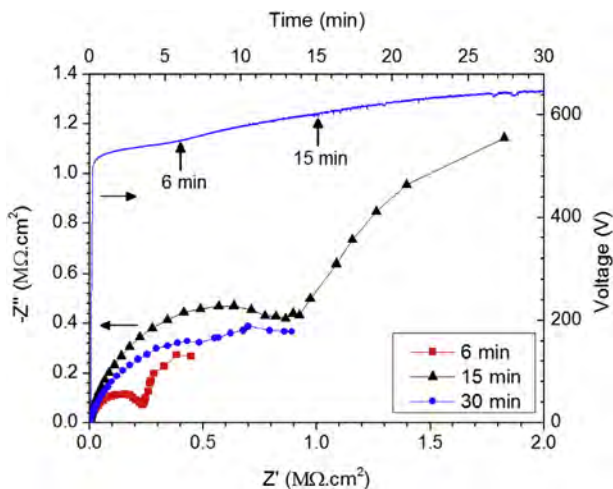


Fig. 9. Nyquist plots recorded after 2 h exposure to 3.5% NaCl for various growth periods, two of which are indicated on the voltage-time response for the S12-15 set of electrical conditions (Table 1). The frequencies at which the last point of the first arc was recorded for samples coated for 6, 15 and 30 min, are 1, 1, and 0.658 Hz, respectively.

set of conditions (Table 1), coatings were grown for 6 min (end of stage 2) and 15 min (end of stage 3) as shown in Fig. 9. The coating grown for the full 30 min was in stage 4. The Nyquist plots recorded on these three coatings are also shown in Fig. 9 and the parameters determined from fits to the electrical equivalent circuit in Fig. 3 are listed in Table 3. Also shown in Table 3 are the R_p values obtained from LPR measurements.

These results show that the sample coated for 6 min (i.e., to the end of stage 2, Fig. 9) exhibited the lowest resistances (R_1 and R_2) while that coated for 15 min (i.e., to the end of stage 3) had the highest resistances. The average coating thickness after 6, 15, and 30 min was measured to be 3.2, 12.1 and 32.2 μm , respectively, confirming that the coating thickness was not a key factor determining the corrosion resistance.

To confirm whether the surface morphology, and especially the properties of the craters formed, was the key feature controlling the corrosion resistance, coatings were grown for various times ranging from 4 to 30 min using the S12-20 set of electrical parameters (Table 1). The SEM micrographs for four of these coatings are shown in Fig. 10. The voltage-time response curve and measured radii of the craters are plotted in Fig. 11. The size of the craters was determined from the SEM images using image analysis software.

The coating formed for 4 min contains many open micropores (Fig. 10-a), and was in stage 2 when growth was stopped. After 13 min of growth, the coating was in stage 3. No open micropores appeared visible on the surface of the coating (Fig. 10-b) and there were many small craters. When the growth time was extended to 20 min the sample was at the beginning of stage 4 with bigger craters and some areas of the surface were covered by the nodular structure. After 30 min, when the coating is in stage 4, the craters are significantly bigger and the nodular structure occupied a larger area of the surface.

The average radius of the craters on the PEO coatings for sample S12-20, coated for 6 min, was $7.3 \mu\text{m}$ which increased to $15.4 \mu\text{m}$ after 30 min, implying that micro-discharges became stronger with increasing coating process time.

These results show that the large number of open micropores present in the coatings, formed in Stage 2, contributes significantly to the poor corrosion resistance.

Inspection of the EIS and LPR results in Table 2, the voltage-time curves in Figs. 1 and 2, and the variation in crater size of the PEO coatings with deposition time, Fig. 11, indicates that samples which spent more time in stage 4 generally show a lower value of R_2 compared to the samples coated in stage 3. The improved corrosion resistance of the coatings formed in Stage 3 can be partly attributed to the presence of small craters with tight discharge channels, reflecting the presence of micro-discharges with moderate intensity, and partly to a more corrosion resistant inner barrier coating, suggested by higher R_2 values. When the coating process is extended to Stage 4, the presence of large craters with wider discharge channels created by strong micro-discharges, negatively affects the corrosion protection of coatings by influencing both the outer functional and the inner barrier layer. The higher values of R_2 compared to R_1 suggest the barrier layer is the major contributor to corrosion protection in PEO coatings. Inspection of the cross-sectional elemental maps of S18-10 and S18-20 in which PEO

Table 3

Polarization resistance (R_p) values and electrical parameters from fits of EIS plots for coatings on 6061 Al alloys after 2 h of exposure to 3.5 wt% NaCl.

Sample	CPE1-Q ($\mu\text{F}/\text{cm}^2 \text{s}^{n-1}$)	CPE1-n	R1 ($\text{M}\Omega \text{ cm}^2$)	CPE2-Q ($\mu\text{F}/\text{cm}^2 \text{s}^{n-1}$)	CPE2-n	R2 ($\text{M}\Omega \text{ cm}^2$)	R_p ($\text{M}\Omega \text{ cm}^{2a}$)
S12-15-6 min	0.202	0.84	0.297	4.260	-1	0.403	0.460
S12-15-15 min	0.065	0.87	1.116	0.734	-1	1.915	1.859
S12-15-30 min	0.347	0.79	0.882	3.241	-1	0.374	1.058

^a Extracted from linear polarization test results.

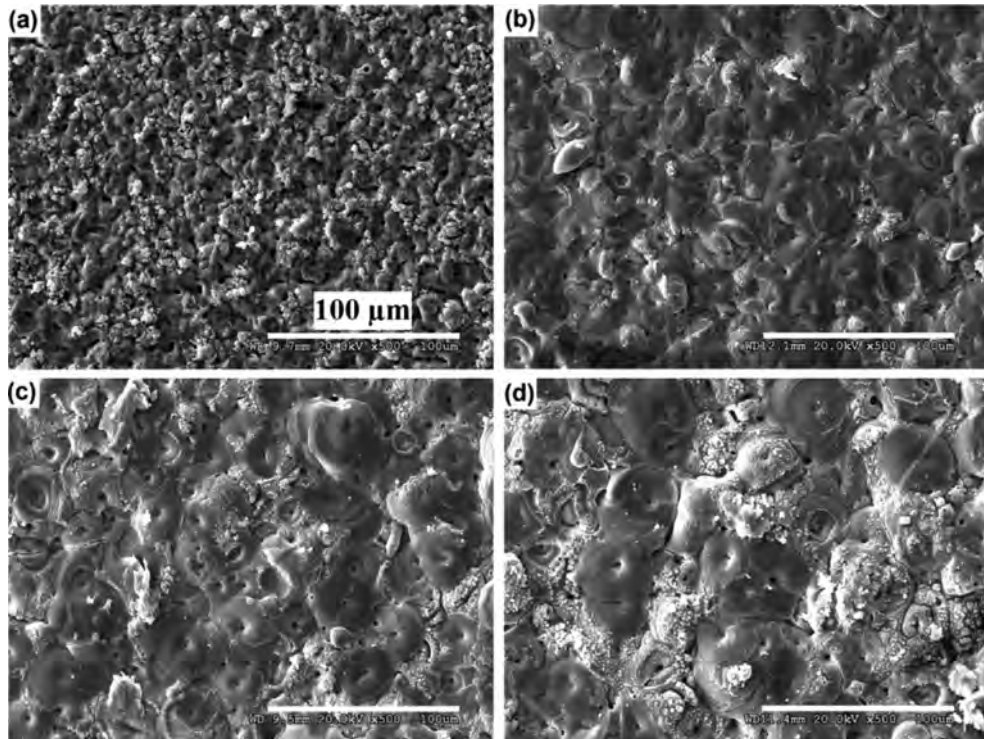


Fig. 10. SEM micrographs of the free surface of S12-20 samples (Table 1) coated at different processing times and stages: (a) 4 min, stage 2; (b) 13 min, stage 3; (c) 20 min, beginning of stage 4; (d) 30 min, stage 4.

coating was stopped in stage 3 and 4, respectively, and comparison of the R_2 values obtained from EIS measurements of samples coated in the different stages of the PEO process, Table 2, suggest that the stage of the PEO process affects the characteristics of both the functional and barrier layer.

Information about the correlation between PEO processing parameters and the integrity and compactness of the coating barrier layer is scarce in the literature and a more detailed study is required to examine how the characteristics of the barrier layer are influenced by the stage of the PEO process. A possibility is that the presence of Si in the barrier layer, as observed for S18-20, is an indication of the presence of mullite ($3\text{Al}_2\text{O}_3 \cdot 2\text{SiO}_2$), a phase which does not form a coherent layer when present at the functional layer/solution interface [10]. It is possible its incorporation into the barrier layer in Stage 4 leads to a similar degradation of this layer.

4. Summary and conclusions

PEO coatings were produced on the 6061 aluminium alloy using different processing parameters under galvanostatic control. The corrosion performance of the coatings was evaluated using EIS and LPR.

The primary influence on corrosion performance was the stage within which the coatings were produced. This controlled the morphology of the coatings and was determined by the process parameters.

The coating thickness and phase composition were found not to have any significant influence on corrosion resistance.

The surface morphologies of samples coated in stage 2 contained many open micro-pores resulting in the very poor corrosion resistance.

In stage 3, the coating surface was composed of small craters with very small discharge channels and the corrosion resistance improved.

In stage 4 the size of the craters and discharge channels increased, thus negatively affecting the corrosion protection of coatings.

Samples coated at the end of stage 3 and the beginning of stage 4 generally demonstrated better corrosion properties.

The improved corrosion performance of samples coated in stage 3 is attributed to micro-discharges with moderate intensity that create fine craters with small discharge channels on the surface of the samples and also to a barrier layer with a higher corrosion resistance compared to coatings completed in stage 2 and 4.

Acknowledgements

The authors would like to thank Dr Jamie Noel for his help and useful comments on the electrochemical tests.

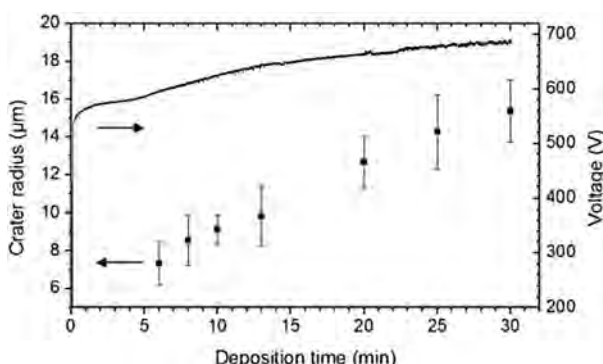


Fig. 11. Variation in crater size of the PEO coatings on 6061 Al alloy substrate as a function of deposition time in sample S12-20 (Table 1). The voltage-time response for these conditions is also shown.

References

- [1] R.O. Hussein, D.O. Northwood, X. Nie, The effect of processing parameters and substrate composition on the corrosion resistance of plasma electrolytic oxidation (PEO) coated magnesium alloys, *Surf. Coatings Technol.* 237 (2013) 357–368.
- [2] X. Nie, E.I. Meletis, J.C. Jiang, A. Leyland, A.L. Yerokhin, A. Matthews, Abrasive wear/corrosion properties and TEM analysis of Al_2O_3 coatings fabricated using plasma electrolysis, *Surf. Coat. Technol.* 149 (2002) 245–251.
- [3] D. Sreekanth, N. Rameshababu, K. Venkateswarlu, Effect of various additives on morphology and corrosion behavior of ceramic coatings developed on AZ31 magnesium alloy by plasma electrolytic oxidation, *Ceram. Int.* 38 (2012) 4607–4615.
- [4] M. Shokouhfar, C. Dehghanian, M. Montazeri, A. Baradaran, Preparation of ceramic coating on Ti substrate by plasma electrolytic oxidation in different electrolytes and evaluation of its corrosion resistance: part II, *Appl. Surf. Sci.* 258 (2012) 2416–2423.
- [5] Y. Cheng, E. Matykina, R. Arrabal, P. Skeldon, G.E. Thompson, Plasma electrolytic oxidation and corrosion protection of Zircaloy-4, *Surf. Coatings Technol.* 206 (2012) 3230–3239.
- [6] V. Dehnavi, B.L. Luan, D.W. Shoesmith, X.Y. Liu, S. Rohani, Effect of duty cycle and applied current frequency on plasma electrolytic oxidation (PEO) coating growth behavior, *Surf. Coatings Technol.* 226 (2013) 100–107.
- [7] C.S. Dunleavy, I.O. Golosnoy, J.A. Curran, T.W. Clyne, Characterisation of discharge events during plasma electrolytic oxidation, *Surf. Coatings Technol.* 203 (2009) 3410–3419.
- [8] R.H.U. Khan, A. Yerokhin, X. Li, H. Dong, A. Matthews, Surface characterisation of DC plasma electrolytic oxidation treated 6082 aluminium alloy: effect of current density and electrolyte concentration, *Surf. Coatings Technol.* 205 (2010) 1679–1688.
- [9] D.S. Doolabi, M. Ehteshamzadeh, S.M.M. Mirhosseini, Effect of NaOH on the structure and corrosion performance of alumina and silica PEO coatings on aluminum, *J. Mater. Eng. Perform.* 21 (2012) 2195–2202.
- [10] V. Dehnavi, X.Y. Liu, B.L. Luan, D.W. Shoesmith, S. Rohani, Phase transformation in plasma electrolytic oxidation coatings on 6061 aluminum alloy, *Surf. Coat. Technol.* 251 (2014) 106–114.
- [11] R.O. Hussein, X. Nie, D.O. Northwood, Influence of process parameters on electrolytic plasma discharging behaviour and aluminum oxide coating microstructure, *Surf. Coatings Technol.* 205 (2010) 1659–1667.
- [12] R.O. Hussein, P. Zhang, X. Nie, Y. Xia, D.O. Northwood, The effect of current mode and discharge type on the corrosion resistance of plasma electrolytic oxidation (PEO) coated magnesium alloy AJ62, *Surf. Coatings Technol.* 206 (2011) 1990–1997.
- [13] H. Wu, J. Wang, B.B. Long, Z. Jin, W. Naidan, F. Yu, et al., Ultra-hard ceramic coatings fabricated through microarc oxidation on aluminium alloy, *Appl. Surf. Sci.* 252 (2005) 1545–1552.
- [14] R.O. Hussein, X. Nie, D.O. Northwood, A. Yerokhin, A. Matthews, Spectroscopic study of electrolytic plasma and discharging behaviour during the plasma electrolytic oxidation (PEO) process, *J. Phys. D. Appl. Phys.* 43 (2010) 105203–105216.
- [15] J.M. Wheeler, J.A. Curran, S. Shrestha, Microstructure and multi-scale mechanical behavior of hard anodized and plasma electrolytic oxidation (PEO) coatings on aluminum alloy 5052, *Surf. Coatings Technol.* 207 (2012) 480–488.
- [16] J. Behin, S.S. Bakhari, V. Dehnavi, H. Kazemian, S. Rohani, Using coal fly ash and wastewater for microwave synthesis of LTA zeolite, *Chem. Eng. Technol.* 37 (2014) 1–10.
- [17] F.C. Walsh, C.T.J. Low, R.J.K. Wood, K.T. Stevens, J. Archer, A.R. Poeton, et al., Plasma electrolytic oxidation (PEO) for production of anodised coatings on lightweight metal (Al, Mg, Ti) alloys, *Trans. Inst. Met. Finish.* 87 (2009) 122–135.
- [18] Y. Liu, J. Xu, Y. Gao, Y. Yuan, C. Gao, Influences of additive on the formation and corrosion resistance of micro-arc oxidation ceramic coatings on aluminum alloy, *Phys. Procedia* 32 (2012) 107–112.
- [19] A.A. Voevodin, A.L. Yerokhin, V.V. Lyubimov, M.S. Donley, J.S. Zabinski, Characterization of wear protective Al-Si-O coatings formed on Al-based alloys by micro-arc discharge treatment, *Surf. Coat. Technol.* 86–87 (1996) 516–521.
- [20] A.L. Yerokhin, A.A. Voevodin, V.V. Lyubimov, J. Zabinski, M. Donley, Plasma electrolytic fabrication of oxide ceramic surface layers for tribotechnical purposes on aluminium alloys, *Surf. Coat. Technol.* 110 (1998) 140–146.
- [21] J.B. Bajat, R. Vasilic, S. Stojadinovic, V. Miskovic-Stankovic, Corrosion stability of oxide coatings formed by plasma electrolytic oxidation of aluminum: optimization of process time, *Corrosion* 69 (2013) 693–702.
- [22] V. Dehnavi, B.L. Luan, X.Y. Liu, D.W. Shoesmith, S. Rohani, Correlation between plasma electrolytic oxidation treatment stages and coating microstructure on aluminum, *Surf. Coat. Technol.* 269 (2015) 91–99.
- [23] R.C. Barik, J.A. Wharton, R.J.K. Wood, K.R. Stokes, R.L. Jones, Corrosion, erosion and erosion–corrosion performance of plasma electrolytic oxidation (PEO) deposited Al_2O_3 coatings, *Surf. Coatings Technol.* 199 (2005) 158–167.
- [24] E. Matykina, R. Arrabal, D.J. Scurr, A. Baron, P. Skeldon, G.E. Thompson, Investigation of the mechanism of plasma electrolytic oxidation of aluminium using 180 tracer, *Corros. Sci.* 52 (2010) 1070–1076.
- [25] E. Matykina, R. Arrabal, P. Skeldon, G.E. Thompson, Investigation of the growth processes of coatings formed by AC plasma electrolytic oxidation of aluminium, *Electrochim. Acta* 54 (2009) 6767–6778.
- [26] L. Wen, Y. Wang, Y. Zhou, L. Guo, J.-H. Ouyang, Microstructure and corrosion resistance of modified 2024 Al alloy using surface mechanical attrition treatment combined with microarc oxidation process, *Corros. Sci.* 53 (2011) 473–480.
- [27] C.E. Barchiche, D. Veys-Renaux, E. Rocca, A better understanding of PEO on Mg alloys by using a simple galvanostatic electrical regime in a KOH–KF– Na_3PO_4 electrolyte, *Surf. Coatings Technol.* 205 (2011) 4243–4248.
- [28] N.M. Alanazi, A. Leyland, A.L. Yerokhin, A. Matthews, Substitution of hexavalent chromate conversion treatment with a plasma electrolytic oxidation process to improve the corrosion properties of ion vapour deposited AlMg coatings, *Surf. Coatings Technol.* 205 (2010) 1750–1756.
- [29] H. Fadaee, M. Javidi, Investigation on the corrosion behaviour and microstructure of 2024-T3 Al alloy treated via plasma electrolytic oxidation, *J. Alloys Compd.* 604 (2014) 36–42.
- [30] A. Venugopal, R. Panda, S. Manwatkar, K. Sreekumar, L.R. Krishna, G. Sundararajan, Effect of micro arc oxidation treatment on localized corrosion behaviour of AA7075 aluminum alloy in 3.5% NaCl solution, *Trans. Nonferrous Met. Soc. China* 22 (2012) 700–710.
- [31] X. Zhang, Y. Zhang, L. Chang, Z. Jiang, Z. Yao, X. Liu, Effects of frequency on growth process of plasma electrolytic oxidation coating, *Mater. Chem. Phys.* 132 (2012) 909–915.
- [32] H. Guo, Y. Ma, J. Wang, Y. Wang, H. Dong, Y. Hao, Corrosion behavior of microarc oxidation coating on AZ91D magnesium alloy in NaCl solutions with different concentrations, *Trans. Nonferrous Met. Soc. China* 22 (2012) 1786–1793.
- [33] J. Lee, Y. Kim, W. Chung, Effect of Ar bubbling during plasma electrolytic oxidation of AZ31B magnesium alloy in silicate electrolyte, *Appl. Surf. Sci.* 259 (2012) 454–459.
- [34] M. Shokouhfar, C. Dehghanian, A. Baradaran, Preparation of ceramic coating on Ti substrate by plasma electrolytic oxidation in different electrolytes and evaluation of its corrosion resistance, *Appl. Surf. Sci.* 257 (2011) 2617–2624.
- [35] M. Chen, S. Liu, J. Li, N. Cheng, X. Zhang, Improvement to corrosion resistance of MAO coated 2519 aluminum alloy by formation of polypropylene film on its surface, *Surf. Coatings Technol.* 232 (2013) 674–679.
- [36] A.L. Yerokhin, L.O. Snizhko, N.L. Gurevina, A. Leyland, A. Pilkington, A. Matthews, Discharge characterization in plasma electrolytic oxidation of aluminium, *J. Phys. D. Appl. Phys.* 36 (2003) 2110–2120.
- [37] F. Xu, Y. Xia, G. Li, The mechanism of PEO process on Al–Si alloys with the bulk primary silicon, *Appl. Surf. Sci.* 255 (2009) 9531–9538.
- [38] Y. Guan, Y. Xia, G. Li, Growth mechanism and corrosion behavior of ceramic coatings on aluminum produced by autocontrol AC pulse PEO, *Surf. Coatings Technol.* 202 (2008) 4602–4612.
- [39] H.M. Nykyforchyn, M.D. Klapiv, V.M. Posuvailo, Properties of synthesised oxide-ceramic coatings in electrolyte plasma on aluminium alloys, *Surf. Coatings Technol.* 100–101 (1998) 219–221.
- [40] L. Wang, X. Nie, Silicon effects on formation of EPO oxide coatings on aluminum alloys, *Thin Solid Films* 494 (2006) 211–218.
- [41] M.M.S. Al Bosta, K. Ma, H. Chien, M.M.S. Al Bosta, The effect of MAO processing time on surface properties and low temperature infrared emissivity of ceramic coating on aluminium 6061 alloy, *Infrared Phys. Technol.* 60 (2013) 323–334.
- [42] G. Sundararajan, L. Rama Krishna, Mechanisms underlying the formation of thick alumina coatings through the MAO coating technology, *Surf. Coatings Technol.* 167 (2003) 269–277.
- [43] S. Moon, Y. Jeong, Generation mechanism of microdischarges during plasma electrolytic oxidation of Al in aqueous solutions, *Corros. Sci.* 51 (2009) 1506–1512.
- [44] S. Stojadinovic, R. Vasilic, I. Belca, M. Petkovic, B. Kasalica, Z. Nedic, et al., Characterization of the plasma electrolytic oxidation of aluminium in sodium tungstate, *Corros. Sci.* 52 (2010) 3258–3265.
- [45] Y. Cheng, F. Wu, E. Matykina, P. Skeldon, G.E. Thompson, The influences of microdischarge types and silicate on the morphologies and phase compositions of plasma electrolytic oxidation coatings on Zircaloy-2, *Corros. Sci.* 59 (2012) 307–315.